

# Investigation of Tire Rotating Modeling Techniques Using Computational Fluid Dynamics<sup>1</sup>

**Gen Fu**

Engineering Science and Mechanics Program,  
Virginia Tech,  
Blacksburg, VA 24061  
e-mail: gen8@vt.edu

**Alexandrina Untaroiu<sup>2</sup>**

Department of Mechanical Engineering,  
Virginia Tech,  
Blacksburg, VA 24061  
e-mail: alexu@vt.edu

*Fuel efficiency becomes very important for new vehicles. Therefore, improving the aerodynamics of tires has started to receive increasing interest. While the experimental approaches are time-consuming and costly, numerical methods have been employed to investigate the air flow around tires. Rotating boundary and contact patch are important challenges in the modeling of tire aerodynamics. Therefore, majority of the current modeling approaches are simplified by neglecting the tire deformation and contact patch. In this study, a baseline computational fluid dynamics (CFD) model is created for a tire with contact patch. To generate mesh efficiently, a hybrid mesh, which combines hex elements and polyhedral elements, is used. Then, three modeling approaches (rotating wall, multiple reference frame, and sliding mesh) are compared for the modeling of tire rotation. Additionally, three different tire designs are investigated, including smooth tire, grooved tire, and grooved tire with open rim. The predicted results of the baseline model agree well with the measured data. Additionally, the hybrid mesh shows to be efficient and to generate accurate results. The CFD model tends to overpredict the drag of a rotating tire with contact patch. Sliding mesh approach generated more accurate predictions than the rotating wall and multiple reference frame approaches. For different tire designs, tire with open rim has the highest drag. It is believed that the methodology presented in this study will help in designing new tires with high aerodynamic performance. [DOI: 10.1115/1.4051311]*

*Keywords: CFD, rotating boundary, tire, aerodynamic performance*

## Introduction

Fuel efficiency is very important when designing new vehicles. During operation, available energy is consumed by aerodynamic drag and rolling resistance. According to previous studies, it is estimated that the aerodynamic drag generated from the tire and rim assembly contributes to 25% of the vehicle aerodynamic drag [1,2]. It is also believed that the tire geometrical design has considerable influences on the aerodynamic performance of the tire [3]. Therefore, the design optimization [4–6] by investigating the aerodynamic drag of tires started to capture interest in the field.

The aerodynamic coefficient of tires can be obtained both experimentally and numerically. While performing wind tunnel tests is costly and time-consuming, computational fluid dynamics (CFD) could be a better alternative. Good correlations between the CFD predictions and experimental data were obtained for a tire simulated statically [7]. The flow around a static Formula 1 tire was simulated using two turbulence-modeling approaches (Reynolds-averaged Navier–Stokes and large eddy simulation). The contact patch was included in the model, and the location of vortex cores behind the tire was predicted [8]. Different front and rear wheel designs in terms of aerodynamic drag were compared [9]. It was concluded that aerodynamic drag can be reduced using different front and rear wheel designs. The effects of different tires showed experimentally to be significant. It was found that grooved tires get lower drag force for a sedan car [10]. Investigations conducted on an isolated tire found that the most important differences between grooved tire and slick tire are pressure

distribution and drag coefficient [11]. A scaled tire model showed to represent accurately a production tire in the experiment. Therefore, it was used then to optimize the aerodynamic performance of a tire without the vehicle [12].

Modeling of tire rotation is a challenging task, so several modeling techniques were investigated in literature. The most popular approaches include sliding mesh [13], moving wall, multiple reference frames [14], and immersed boundary. In a study [13], it was shown that sliding mesh has better predictions than rotating wall, but the CFD model showed poor correlation relative to particle image velocimetry results. The lattice Boltzmann method was also used to simulate the rotating tire tread. Compared to rotating wall boundary condition, it showed better agreement with the experimental wake survey behind the tire. Overall, previous studies mostly used only one rotating modeling approach. While a few studies have compared different approaches, they used undeformed tires. Therefore, it would be interesting to know how different rotating approaches affect the modeling of tires with contact patch. Additionally, the effect of open rim on the aerodynamic performance of a stand-alone tire has not been explicitly investigated yet.

The main objective of this study is to create a baseline CFD model for a single tire with contact patch and validate it with experimental data. In the process, three rotation-modeling approaches are compared and analyzed. The aerodynamic drag of the tire is used as the major indicator of the tire aerodynamic performance. A hybrid mesh is used to show its ability to represent the sharp edge and large curvature around the contact patch.

## Numerical Model

In this study, a three-dimensional (3D) CFD model was created around a tire (Fig. 1(a)) using ANSYS FLUENT 2020R2. In order to anchor the numerical results, the tire size (225/55 R17) is the same as references [15,16]. The deformed tire shape was calculated using an finite element model provided by Nexen Tire

<sup>1</sup>Paper presented in part at the FEDSM 2020 Fluids Engineering Conference, Virtual, July 13–15, 2020, Paper no. FEDSM2020-11936. The author was selected as a graduate scholar of the conference.

<sup>2</sup>Corresponding author.

Contributed by the Fluids Engineering Division of ASME for publication in the JOURNAL OF FLUIDS ENGINEERING. Manuscript received February 3, 2021; final manuscript received May 24, 2021; published online July 2, 2021. Assoc. Editor: Ning Zhang.

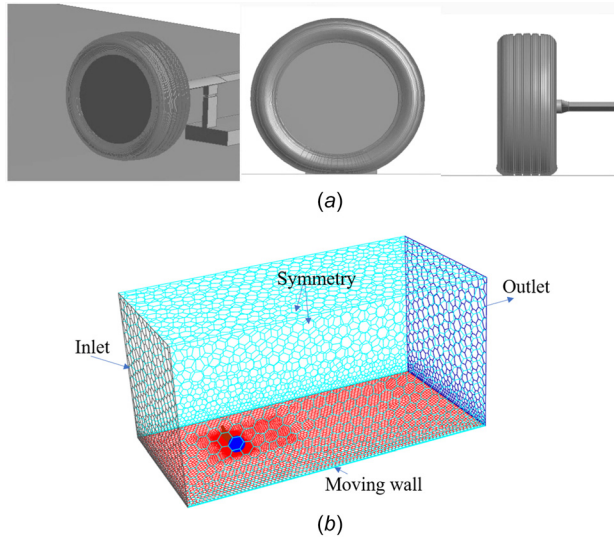


**Fig. 1** Geometry and boundary conditions of the CFD (a) tire size (225/55R17) and (b) fluid domain

(Yangsang-si, South Korea) using ABAQUS 2020. The boundary set up for the CFD model was applied (Fig. 1(b)). The parameters used in the CFD model are listed in Table 1 [17]. Due to the periodicity of the tire rotating process, a 1 s simulation showed to be sufficient for the objective of this study [15,16].

**Turbulence Model.** In the baseline model, renormalization Group (RNG)- $k$ - $\epsilon$  model, developed based on the Boussinesq approximation, is used [15]. The isotropic Reynolds stress can be written in the form of a turbulent viscosity of the fluid as

$$\tau_{ij} = 2\mu_t S_{ij} - \frac{2}{3} \left( \mu_t \frac{\partial V_i}{\partial V_i} \right) \delta_{ij} \quad (1)$$

The turbulent viscosity can be calculated from turbulent kinetic energy and dissipation

$$\mu_t = \rho \frac{C_\mu k^2}{\epsilon} \quad (2)$$

$k$  can be derived using transport equations

$$\rho \frac{Dk}{Dt} = \frac{\partial}{\partial x_j} \left[ \left( \frac{\mu_0}{\delta_{k0}} + \frac{\mu_t}{\delta_{kt}} \right) \frac{\partial k}{\partial x_j} \right] + \tau_{ij} S_{ij} - \rho \epsilon \quad (3)$$

**Table 1** Parameter used in CFD model

Properties	Value
Turbulence model	$k$ - $\epsilon$
Turbulence intensity and length scale	0.2%, 3 mm
Formulation	URANS
Wall treatment	Enhanced
Rotation model	Rotating wall, sliding mesh
Solver	SIMPLE, compressible
Internal iterations per time step	5
Under-relaxation speed/pressure/turbulence	0.8/0.2/0.8
Time discretization	Second order
Time step	$10^{-4}$ s
Solution time	1.0 s
Convergence criteria	$10 \times 10^{-4}$
Height of the first prism layer on the wheel	0.015 mm

URANS: unsteady Reynolds-averaged Navier–Stokes.

$$\rho \frac{D\epsilon}{Dt} = \frac{\partial}{\partial x_j} \left[ \left( \frac{\mu_0}{\delta_{\epsilon 0}} + \frac{\mu_t}{\delta_{\epsilon t}} \right) \frac{\partial \epsilon}{\partial x_j} \right] + C_{\epsilon 1} \frac{\epsilon}{k} \tau_{ij} S_{ij} - \left( C_{\epsilon 2} + C_\mu \frac{\eta^3 (1 - \eta/\eta_0)}{1 + \beta \eta^3} \right) \rho \frac{\epsilon^2}{k} \quad (4)$$

The empirical coefficients are  $C_\mu = 0.085$ ,  $C_{\epsilon 1} = 1$ ,  $C_{\epsilon 2} = 1.68$ ,  $\delta_{k0} = \delta_{\epsilon 0} = \delta_{\epsilon t} = \delta_{kt} = 0.719$ ,  $\eta_0 = 4.38$ ,  $\beta = 0.012$  [15,16].

Wall functions are semi-empirical formulas and functions used to model the near wall region. They connect the solution variables at near wall cells with the quantities on the wall. In this approach, wall functions are used to bridge the viscosity-affected region between the wall and the fully turbulent region. In such case, turbulence model does not need to be changed to consider the effect of the wall [18]. The drawback of wall function is the error in wall shear stress and wall heat transfer from refined mesh near the wall. It is known that the accuracy of numerical results can deteriorate if  $y^+$  value is too small. However, FLUENT provides  $y^+$  value insensitive formulations for wall function in  $\omega$  based and  $\epsilon$  based turbulence equations. The turbulence viscosity has a maximum in the middle of the boundary layer.

**Mesh Generation.** A hybrid mesh, which consists in polyhedral mesh on all the boundaries and hex elements inside the volume, was used in this model (Fig. 2(a)). The mesh quality around the sharp corner of the contact patch was improved using a step (Fig. 2(b)) [17].

**Tire Rotation Modeling Approaches.** Three rotating tire rotation-modeling approaches are investigated in this study.

**Rotating Wall Approach.** In this approach, a rotational speed is defined on a moving surface boundary. The cell velocities on the surface are determined by multiplying the angular speed with the distance [19]. Only the tangential component can be applied to the wall, so the normal component of the velocity is removed. When the rotating velocity is normal to the surface boundary, the rotating wall approach is not valid. As a result, it is not feasible to use rotating wall approach on spokes and lateral grooves. The conversion from translate velocity to rotating velocity is made using Eq. (5) (Fig. 3)

$$\omega = \frac{\Delta\theta}{\Delta t} = 2 \arctan \left( \frac{\frac{1}{2} \Delta x_{\text{flat}}}{r} \right) \frac{v}{\Delta x_{\text{flat}}} \quad (5)$$

**Moving Reference Frame Approach.** In this approach, different zones are set to different speeds, including rotational and translational speeds. Moving reference frame (MRF) equations are solved in these zones. The flow parameters are transformed at the interfaces so that they can be used to calculate the fluxes at the boundary of the adjacent zone.

A separated flow region is set to a rotating frame in this method, where the geometry does not actually move. The rim remains in the initial position. Centrifugal and Coriolis acceleration are represented as volume forces, which are transformed into a rotating reference frame. In this case, the tire surface is part of the moving reference frame being inside the rotating region, which is defined by the user. In FLUENT software, the coordinate system of the rotating region is rotating with an angular velocity  $\omega$ . The vector  $r$  represents the relative location of the two systems. The velocity in rotating frame can be written as

$$\mathbf{V}_r + \omega \times \mathbf{r} = \mathbf{V} \quad (6)$$

where  $\mathbf{V}_r$  is the velocity in rotating frame,  $\mathbf{V}$  is the absolute velocity viewed from stationary frame,  $\omega \times \mathbf{r}$  represent the velocity of the rotating frame relative to the inertial reference frame.

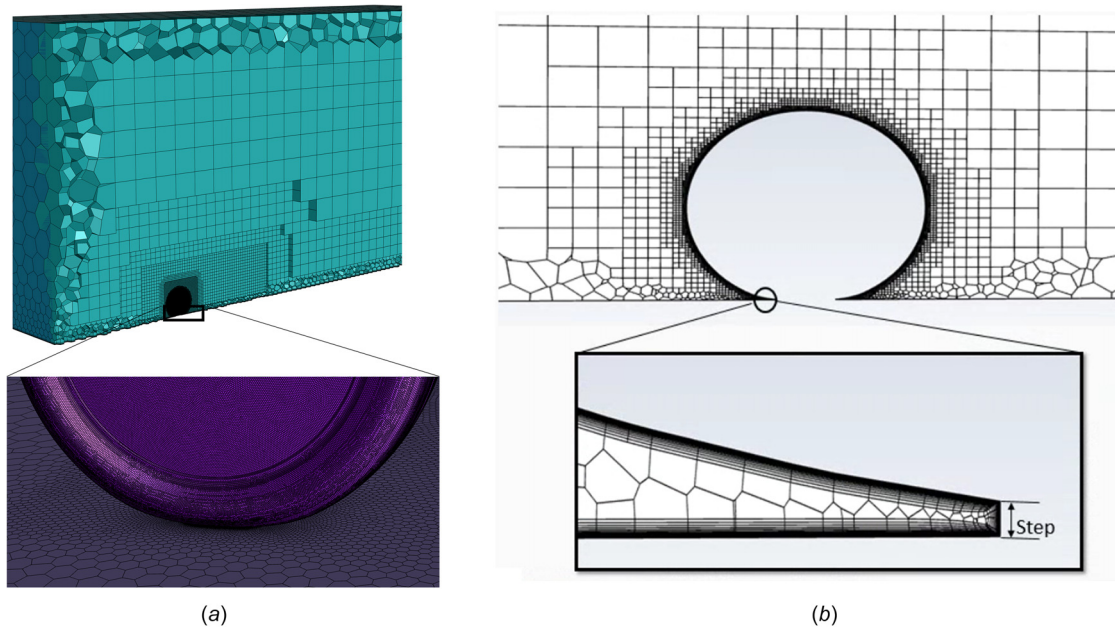


**Fig. 2 Mesh generation (a) hybrid mesh elements and (b) cross section of the mesh**

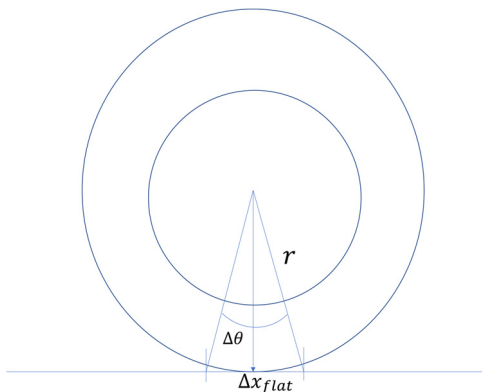


**Fig. 3 Conversion of translational velocity and rotating speed**

In the tire CFD model, the rotating domain is small compared with the whole computational domain. Using absolute velocity formulation is recommended to reduce the numerical diffusion in the solution. The absolute velocity formulations are shown as follows:

Conservation of mass

$$\frac{\partial \rho}{\partial t} + \nabla \cdot \rho \mathbf{V}_r = 0 \quad (7)$$

Conservation of momentum

$$\frac{\partial \rho}{\partial t} \rho \mathbf{V}_r + \nabla \cdot (\rho \mathbf{V}_r \mathbf{V}) + \rho (\boldsymbol{\omega} \times \mathbf{r}) = -\nabla p + \nabla \cdot \boldsymbol{\tau} + \mathbf{F} \quad (8)$$

In the momentum equation, Coriolis acceleration and centripetal acceleration are combined in one term.

*Sliding Mesh Approach.* Sliding mesh is a transient process, which contains actual rotation of a partial grid. In the simulation, the rotating zone rotates in respect to the global static frame at tire speed. The value on the interface is transferred between grids using a rotationally symmetric property. The position of the interfaces has influence on the results. The conservation equation for a

general scalar on an arbitrary control volume  $V$ , which has a sliding boundary, is shown as

$$\frac{d}{dt} \int_V \rho \phi dV + \int_{\partial V} \rho \phi (\mathbf{V} - \mathbf{V}_g) dA = \int_{\partial V} \Gamma \nabla \phi dA + \int_V S_\phi dV \quad (9)$$

where  $\rho$  is the density,  $\mathbf{V}$  is the flow velocity,  $\mathbf{V}_g$  is the mesh velocity of the moving boundary,  $\Gamma$  is the diffusion coefficient,  $S_\phi$  is the source term of  $\phi$ , and  $\partial V$  is the boundary of the control volume  $V$ .

Time derivative term can be written as

$$\frac{d}{dt} \int_V \rho \phi dV = \frac{\rho \phi V^{n+1} - \rho \phi V^n}{\Delta t} \quad (10)$$

Since the volume stays constant, the following equations can be derived for the transient term in sliding mesh approach:

$$V^{n+1} = V^n \quad (11)$$

$$\frac{dV}{dt} = 0 = \int_{\partial V} \mathbf{V}_g dA = \sum \mathbf{V}_{gi} A_i \quad (12)$$

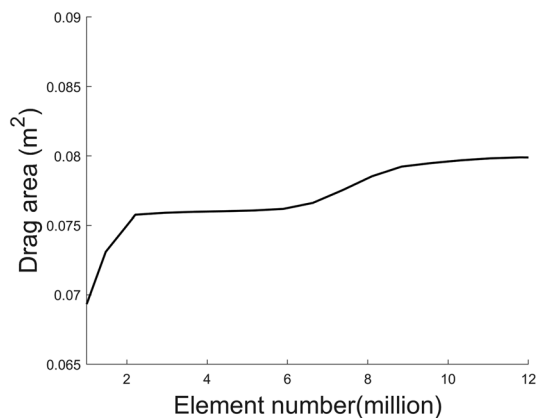


**Fig. 4 Grid convergence study**

**Table 2 Error analysis**

Critical variable	Drag area
Three mesh densities	6, 9, 12 (million)
$GCI_{\text{fine}}$	0.66%
Uncertainty of drag area	$\pm 0.00052$

$$\frac{d}{dt} \int_V \rho \phi dV = \frac{[\rho \phi^{n+1} - \rho \phi^n] V}{\Delta t} \quad (13)$$

**Results and Discussion**

**Baseline Model Validation.** In order to select an optimal grid density, a grid independence study was conducted. Drag area of the tire is used as an indicator for different mesh densities. As it can be observed (Fig. 4), a plateau region occurs after about

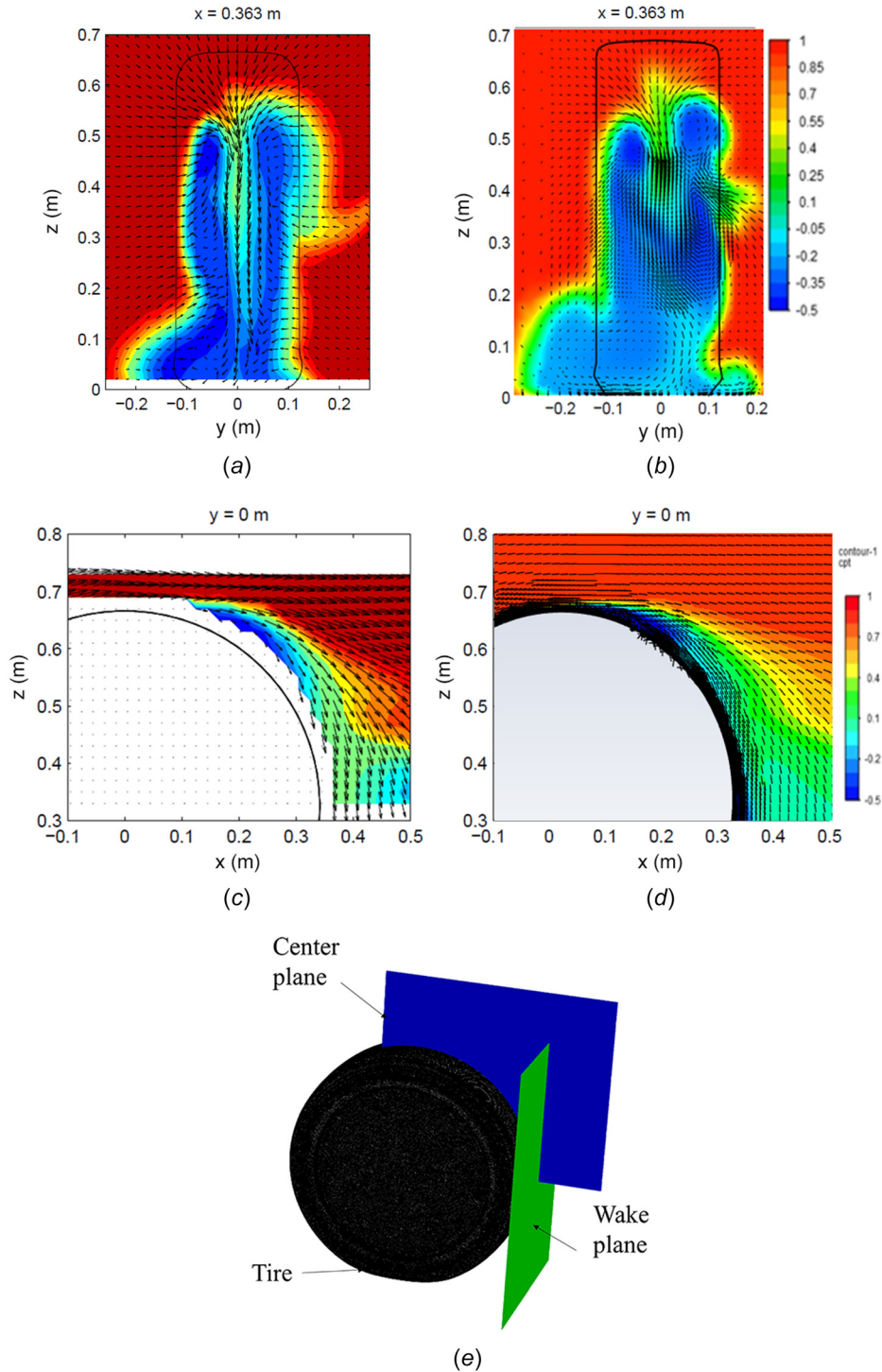


**Fig. 5** Smoothed tire with groove experiment [15]: (a) reference, (b) CFD, (c) reference, (d) CFD, and (e) measuring planes

**Table 3 Drag area for smooth tire with grooves**

Drag area $C_dA$ (m <sup>2</sup> )	Smooth tire with grooves	Absolute percentage error (%)
Experiment [15]	0.063	
Reference numerical [15]	0.080	26.9
CFD	0.076	20.6

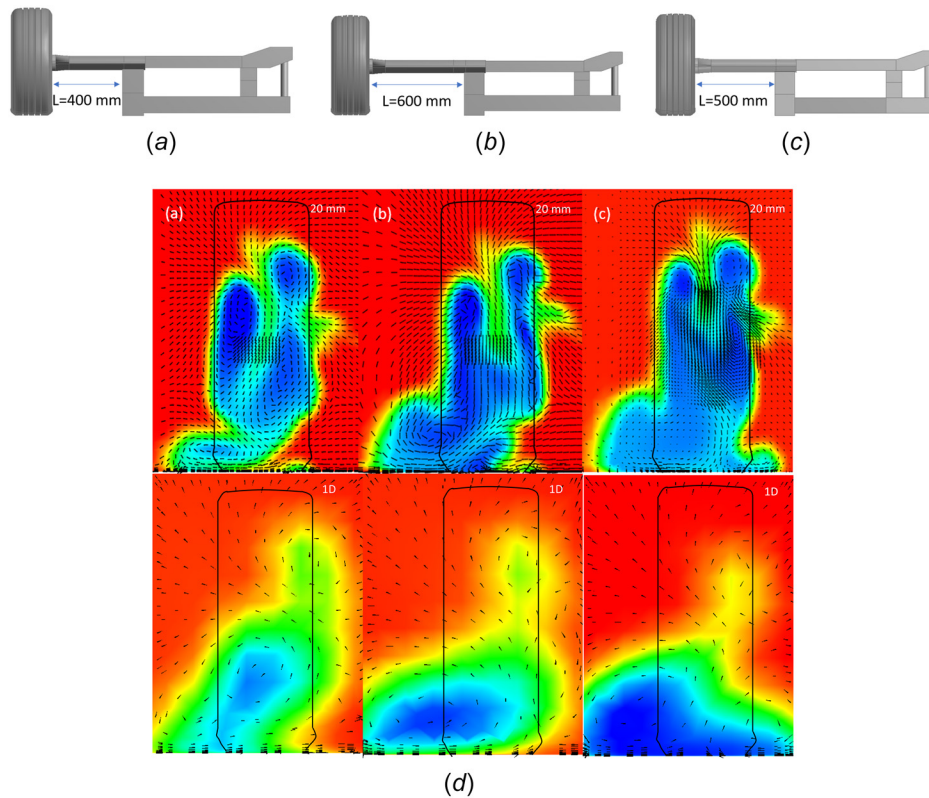


**Fig. 6 Wake profile of different shaft dimensions (a) fixture size 1,  $L = 400$  mm, (b) fixture size 3,  $L = 600$  mm, (c) fixture size 3,  $L = 500$  mm, and (d) wake profiles at 20 mm and 1 tire diameter (1D) downstream**

$9 \times 10^6$  elements in terms of drag area. Therefore, a final mesh density of  $9 \times 10^6$  was chosen for the baseline model.

The numerical uncertainty of baseline model was analyzed as well. A method based on Richardson extrapolation was used to estimate the discretization error [20]. Grid convergence index (GCI) is calculated (Table 2).

The baseline model is also validated against experimental data from Ref. [15]. The wind tunnel tests were conducted in AEROLAB at BMW. The tire of dimension 225/55 R17 was tested. In the wind tunnel test, the tires were mounted support stings with steel frames. The pressure profiles were measured using a twelve-hole probe. The measuring planes are displayed in Fig. 5(e). The baseline tire has a closed rim and four rain grooves on tire surface (Fig. 1(a)). The total pressure coefficient distribution on center plane and wake plane obtained from CFD simulation (Figs. 5(a) and 5(c)) are compared with the corresponding data recorded in wind tunnel tests (Figs. 5(b) and 5(d)). It can be seen that the numerical predictions and experimental measurements have similar patterns. The CFD model can also predict well the downward flow near the top of the tire. The main difference is terms of the pattern close to the road. This area is affected by the contact patch of the tire and the fixture. It is believed that the difference is mainly caused by inconsistencies in the fixture geometry and the deformed shape of the tire. Three different fixture geometries are compared to show their effects. The wake patterns are displayed

for different shaft dimensions (Fig. 5). It can be seen that if the dimension of the shaft changes, the corresponding flow pattern near the road is also different. Therefore, this agrees with the previous conclusion that the major difference between the experiment data from the reference and simulation is caused by the fixture dimension.

Drag area, calculated as the product of drag coefficient and front area of the tire, was reported (Table 3). It can be observed that both the prediction from this study and reference are higher than the experimental measurement. This is partially due to the fixtures inside the wind tunnel measurement (Fig. 6). Based on the presented results (Figs. 5 and 6 and Table 3), it could be concluded that the baseline model is validated against the experimental measurements.

In order to further verify the CFD model, a lifted smooth tire case is also compared with the reference. In this case, the smooth tire is lifted above the road. The minimum distance from the tire surface to the road is 5 mm. Sliding mesh and rotating wall techniques are compared using the lifted tire case (Fig. 7). A comparison of drag area is presented as well (Table 4). It can be observed that the predictions agree well with the wind tunnel measurements. The results from current CFD model have better predictions than the reference. Sliding mesh shows closer result than rotating wall approach. This also agrees with previous studies, which showed that sliding mesh provides the best prediction [21].

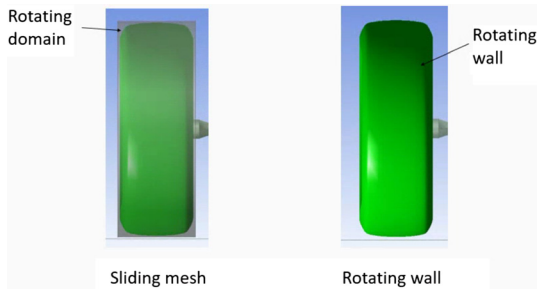


**Fig. 7 Smooth tire, sliding mesh versus rotating wall**

**Table 4 Drag area for smooth tire**

Drag area $C_dA$ (m <sup>2</sup> )	Smooth tire	Absolute percentage error (%)
Experiment [15]	0.068	
Rotating wall	0.071	9.7
Sliding mesh	0.070	9.6
Reference [15]	0.073	10.1

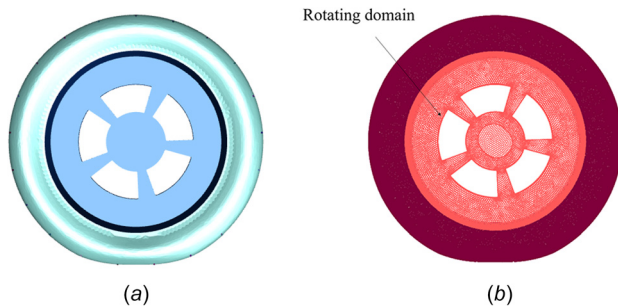


**Fig. 8 Tire with groove and open rim (a) geometry of idealized open rim and (b) location of rotating domain**

**Table 5 Drag area for tire with open rim and longitudinal grooves**

Open rim tire	Drag area $C_dA$ (m <sup>2</sup> )	Ventilation moment of entire tire (N·m)	Ventilation moment of rim (N·m)
Sliding mesh	0.091	1.39	0.49
MRF	0.094	1.26	0.40
Rotating wall	0.092	0.90	0.17

**Rotating Simulation.** After the validation of baseline model, the tire model with an open rim is investigated using rotating wall, sliding mesh and MRF approaches. The sliding mesh and MRF approaches cannot be applied directly to the contact region due to its plane motion relative to the road instead of rotating. Therefore, these approaches were combined with moving wall approach. As a result, in the CFD model, the tire external surface is set as rotating wall while the open rim region is set as a rotating domain. The geometry of this tire model and the location of the rotating domain are shown in Figs. 8(a) and 8(b), respectively.

Three cases, which employ MRF, sliding mesh and rotating wall approaches are compared in this study. In MRF, rotating wall is used on tire external surface, and moving reference frame is applied on the rim region. Similarly, in sliding mesh case, sliding mesh is used on the rim region. In the third case, rotating wall boundary is applied to all tire surfaces. The drag area values and ventilation moments are summarized (Table 5). The predicted drag area from the sliding mesh method is lower than the MRF approach. Based on the results of the baseline model, the CFD model tends to over predict the drag area. Therefore, in this case, it is reasonable to conclude that the sliding mesh approach generates better results, which also agree with previous studies [22–26]. The ventilation moment is the moment caused by aerodynamic resistance, which is also referred as ventilation resistance [2,27] and indicates the effects of tire rotation on the surrounding flow. The ventilation moment of the tire in rotating wall case is much lower than sliding mesh and MRF. The main difference comes from the rim region.

As stated in the methodology section, sliding mesh method is an unsteady simulation, the flow is solved for different rim positions. The elements inside the rotating domain are actually rotating relative to the stationary domain. However, in MRF, an angular velocity vector  $\omega$  is introduced to transform the velocity in the rotating domain. As a result, a pressure gradient is added to the elements which are not strongly affected by rotating parts. This pressure gradient creates discontinuity and errors in these elements. It changes the velocity magnitude of the elements where the flow directions do not align with the axis of rotation [21,28]. It

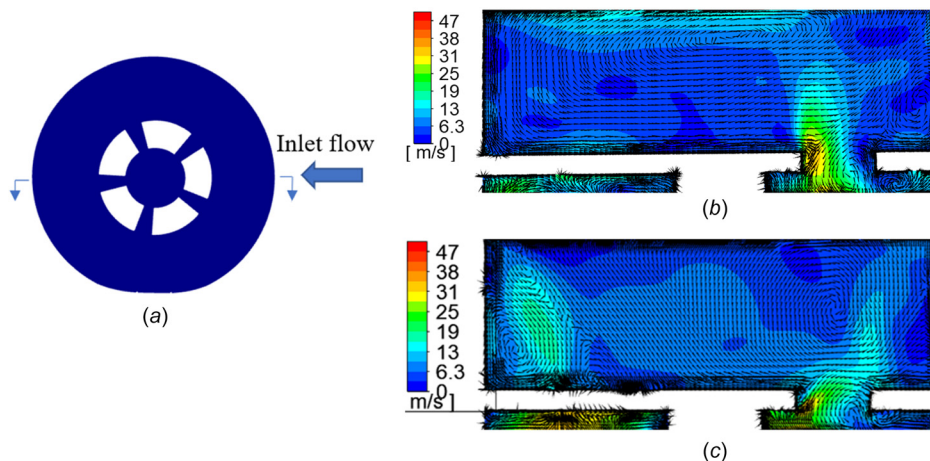


**Fig. 9 Velocity vectors inside the rotating domain for sliding mesh and MRF: (a) location of the cut face, (b) velocity distribution of MRF, and (c) velocity distribution of sliding mesh**

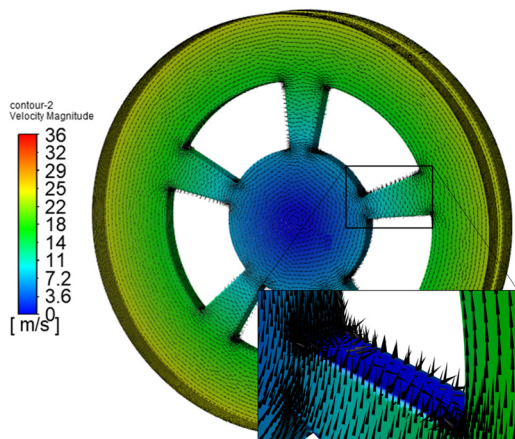


Fig. 10 Velocity vectors on the rim surface using rotating wall

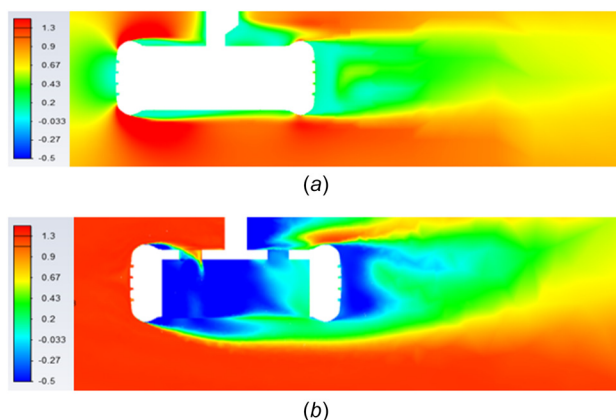


Fig. 11 Total pressure coefficient on the plane slicing through the center of the tire (view from top of the tire) (a) total pressure coefficient contour of close rim (top view) and (b) total pressure coefficient contour of open rim (top view)

can be seen that a large portion of the velocity vectors are in the perpendicular direction of the axis of rotation in MRF case (Fig. 9(c)). These velocity components in the flow then produce unrealistic pressure gradients. Also, the velocity distribution inside the rim region is very different between sliding mesh case and MRF case (Figs. 9(b) and 9(c)).

In rotating wall case, the predicted ventilation moment of the rim region is dramatically lower than the other cases. This is because that velocity components that are normal to the wall boundaries are neglected to satisfy continuity equation. As shown in Fig. 10, there are no velocity components normal to the wall surface can be observed. But, rotating wall method can still predict a drag area which is very close to the sliding mesh case (Table 5). It can be concluded that rotating wall can provide reasonable estimation in terms of aerodynamic drag if the tire geometry has limited surface area that has normal velocity components.

**Influence of Open Rim.** The drag area of the open rim tire is much higher than that of the closed rim comparing the data in Tables 4 and 5. The open rim design increases the total aerodynamic drag of the tire as well. The total pressure plane cutting through the center of the tire horizontally (Fig. 11) shows the details of the behavior around the rim. It can be observed that the flow separates at almost the same location for both cases. However, since the rim forms a cavity, its low pressure region is much larger than in the closed rim case, which explains the higher drag of open rim tire relative to close trim tire.

## Conclusions

In this study, a 3D CFD model is created for an isolated tire. The baseline model is validated by experimental measurements, and then different rotation modeling approaches are compared. CFD model tends to overpredict the drag of a rotating tire with contact patch. Hybrid mesh, which combines polyhedral elements and hex elements, is efficient and can generate accurate results. Discretization error analysis shows good accuracy of the baseline model. The differences of the prediction and experimental data are caused by the uncertainty of the fixture dimension and exact contact shape. Sliding mesh approach can predict more accurate results than the rotating wall and MRF approaches. Rotating wall can also provide more accurate longitudinal drag force prediction than ventilation moment. For a single tire, open rim design can increase the aerodynamic drag.

## Acknowledgment

This work has been partially supported by the Center for Tire Research (CenTiRe), an NSF-I/UCRC (Industry/University Cooperative Research Centers) program led by Virginia Tech. The authors hereby wish to thank the industrial advisory board (IAB) of CenTiRe for their kind support and guidance.

## Funding Data

- NSF (Award Nos. 1650460 and 1650423; Funder ID: 10.13039/100000001).

## Nomenclature

- $C_{\epsilon 2}$  = turbulence model constant
- $C_{\epsilon 1}$  = turbulence model constant
- $C_{\mu}$  = turbulence model constant
- $\mathbf{F}$  = external force
- GCI = grid convergence index
- $k$  = turbulence kinetic energy
- $\mathbf{r}$  = position vector
- $S_{\theta}$  = source term
- $t$  = time
- $\mathbf{V}$  = velocity vector
- $\mathbf{V}_g$  = mesh velocity of the moving boundary
- $\mathbf{V}_r$  = velocity in rotating frame
- $x_j$  = space coordinates
- $y^+$  =  $Y$  plus
- $\beta$  = turbulence model constant
- $\Gamma$  = diffusion coefficient
- $\delta_{kt}$  = turbulence model constant
- $\delta_{k0}$  = turbulence model constant
- $\delta_{\epsilon t}$  = turbulence model constant
- $\delta_{\epsilon 0}$  = turbulence model constant
- $\mu_t$  = turbulence viscosity
- $\epsilon$  = turbulence eddy dissipation
- $\eta_0$  = turbulence model constant
- $\rho$  = density
- $\tau$  = stress tensor
- $\boldsymbol{\tau}$  = isotropic Reynolds stress
- $\boldsymbol{\omega}$  = rotating velocity
- $\varnothing$  = a general scale

## References

- [1] Reiß, J., Haag, L., and Indinger, T., 2019, "CFD Investigation on Fully Detailed and Deformed Car Tires," *Int. J. Autom. Eng.*, **10**(4), pp. 324–331.
- [2] Wickern, G., Zwicker, K., and Pfadenhauer, M., 1997, "Rotating Wheels-Their Impact on Wind Tunnel Test Techniques and On Vehicle Drag Results," SAE Paper No. 970133.
- [3] Alajbegovic, A., Lew, P.-T., Shock, R., Duncan, B., and Hoch, J., 2017, "Aerodynamic Simulation of a Standalone Rotating Tread Tire," *Int. J. Autom. Eng.*, **8**(4), pp. 171–178.
- [4] Fu, G., and Untaroiu, A., 2017, "An Optimum Design Approach for Textured Thrust Bearing With Elliptical-Shape Dimples Using Computational Fluid

- Dynamics and Design of Experiments Including Cavitation,” *ASME J. Eng. Gas Turbines Power*, **139**(9), p. 092502.
- [5] Fu, G., and Untaroiu, A., 2018, “The Influence of Surface Patterning on the Thermal Properties of Textured Thrust Bearings,” *ASME J. Tribol.*, **140**(6), p. 061706.
  - [6] Untaroiu, A., and Fu, G., 2017, “Effect of Recess Shape on the Performance of a High-Speed Hybrid Journal Bearing,” *ASME J. Eng. Gas Turbines Power*, **139**(11), p. 112501.
  - [7] Lounsbury, T. H., Gleason, M. E., Kandasamy, S., Sbeih, K., Mann, R., and Duncan, B. D., 2009, “The Effects of Detailed Tire Geometry on Automobile Aerodynamics—A CFD Correlation Study in Static Conditions,” *SAE Int. J. Passeng. Cars – Mech. Syst.*, **2**(1), pp. 849–860.
  - [8] Axerio, J., Iaccarino, G., Issakhanian, E., Lo, K., Elkins, C., and Eaton, J., 2009, “Computational and Experimental Investigation of the Flow Structure and Vortex Dynamics in the Wake of a Formula 1 Tire,” *SAE Paper No. 2009-01-0775*.
  - [9] Landström, C., Walker, T., Christoffersen, L., and Löfdahl, L., 2011, “Influences of Different Front and Rear Wheel Designs on Aerodynamic Drag of a Sedan Type Passenger Car,” *SAE Paper No. 2011-01-0165*.
  - [10] Landstrom, C., Josefsson, L., Walker, T., and Löfdahl, L., 2012, “Aerodynamic Effects of Different Tire Models on a Sedan Type Passenger Car,” *SAE Int. J. Passeng. Cars-Mech. Syst.*, **5**(1), pp. 136–151.
  - [11] Lesniewicz, P., Kulak, M., and Karczewski, M., 2014, “Aerodynamic Analysis of an Isolated Vehicle Wheel,” *XXI Fluid Mechanics Conference*, Vol. 530, Krakow, Poland, June 15–18, p. 012064.
  - [12] Wittmeier, F., Kuthada, T., Widdecke, N., and Wiedemann, J., 2014, “Model Scale Based Process for the Development of Aerodynamic Tire Characteristics,” *SAE Paper No. 2014-01-0585*.
  - [13] Haag, L., Kiewat, M., Indinger, T., and Blacha, T., 2017, “Numerical and Experimental Investigations of Rotating Wheel Aerodynamics on the Drivetrain Model with Engine Bay Flow,” *ASME Paper No. FEDSM2017-69305*.
  - [14] Lesniewicz, P., Kulak, M., and Karczewski, M., 2016, “Vehicle Wheel Drag Coefficient in Relation to Travelling Velocity - CFD Analysis,” *XXII Fluid Mechanics Conference (KKMP2016)*, Slok near Belchatów, Poland, Sept. 11–14, Vol. 760, p. 012014.
  - [15] Schnepf, B. H., 2014, “Investigation of Influencing Factors on the Flow around a Car Wheel in Simulation and Experiment,” Ph.D. thesis, Technical University of Munich, Munich, Germany.
  - [16] Schnepf, B., Schütz, T., and Indinger, T., 2015, “Further Investigations on the Flow Around a Rotating, Isolated Wheel with Detailed Tread Pattern,” *SAE Int. J. Passeng. Cars - Mech. Syst.*, **8**(1), pp. 261–274.
  - [17] Diasinos, S., Barber, T. J., and Doig, G., 2015, “The Effects of Simplifications on Isolated Wheel Aerodynamics,” *J. Wind Eng. Ind. Aerodyn.*, **146**, pp. 90–101.
  - [18] Ferziger, J. H., Perić, M., and Street, R. L., 2002, *Computational Methods for Fluid Dynamics*, Springer-Vedag Berlin Heidelberg, Germany.
  - [19] Fu, G., Untaroiu, A., and Swanson, E., 2018, “Effect of Foil Geometry on the Static Performance of Thrust Foil Bearings,” *ASME J. Eng. Gas Turbines Power*, **140**(8), p. 082502.
  - [20] Celik, I. B., Ghia, U., Roache, P. J., and Freitas, C. J., 2008, “Procedure for Estimation and Reporting of Uncertainty Due to Discretization in CFD Applications,” *ASME J. Fluids Eng.*, **130**(7), p. 078001.
  - [21] Hobeika, T., Löfdahl, L., and Sebben, S., 2014, “Study of Different Tyre Simulation Methods and Effects on Passenger Car Aerodynamics,” *The International Vehicle Aerodynamics Conference*, H. Park, ed., Woodhead Publishing, Oxford, UK, pp. 187–195.
  - [22] Wäschle, A., 2007, “The Influence of Rotating Wheels on Vehicle Aerodynamics - Numerical and Experimental Investigations,” *SAE Paper No. 2007-01-0107*.
  - [23] Sebben, S., and Mlinaric, P., 2008, “Investigation of the Influence of Tyre Deflection and Tyre Contact Patch on CFD Predictions of Aerodynamic Forces on a Passenger Car,” 7th MIRA International Vehicle Aerodynamics, Nuneaton, UK, Oct., MIRA Ltd.
  - [24] Haag, L., Blacha, T., and Indinger, T., 2017, “Experimental Investigation on the Aerodynamics of Isolated Rotating Wheels and Evaluation of Wheel Rotation Models Using Unsteady CFD,” *Int. J. Autom. Eng.*, **8**(1), pp. 7–14.
  - [25] Chaligné, S., Turner, R., and Gaylard, A., 2017, “The Aerodynamics Development of the New Land Rover Discovery,” *Proceedings of the FKFS Conference*, Springer, Stuttgart, Germany, Sept. 26–27, pp. 145–159.
  - [26] D’Hooge, A., Palin, R. B., Johnson, S., Duncan, B., and Gargoloff, J. I., 2012, “The Aerodynamic Development of the Tesla Model S—Part 2: Wheel Design Optimization,” *SAE Paper No. 2012-01-0178*.
  - [27] Vdovin, A., 2013, “Investigation of Aerodynamic Resistance of Rotating Wheels on Passenger Cars,” Engineering thesis, Department of Applied Mechanics, Chalmers University of Technology, Gothenburg, Sweden.
  - [28] Hobeika, T., and Sebben, S., 2018, “CFD Investigation on Wheel Rotation Modelling,” *J. Wind Eng. Ind. Aerodyn.*, **174**, pp. 241–251.